A&A 474, 229–237 (2007)
DOI: 10.1051/0004-6361:20077308

Astronomy & Astrophysics

Multi-component absorption lines in the *HST* spectra of α Scorpii B⋆

R. Baade and D. Reimers

Hamburger Sternwarte, Gojenbergsweg 112, 21029 Hamburg, Germany
e-mail: rbaade@hs.uni-hamburg.de

Received 15 February 2007 / Accepted 9 July 2007

ABSTRACT

Context. Extended atmospheres of late-type supergiants are of special interest with regard to the mass-loss process, the circumstellar physico-chemistry, and the evolution of stars.
Aims. The circumstellar envelope of α Sco A (M1.5 Iab) has been subject of intensive studies. Nevertheless the mechanism that is responsible for the mass outflow is still poorly understood. High-resolution spectroscopy is required to re-investigate the wind properties of the supergiant.
Methods. We present HST/GHRS observation of α Sco B (B2.5 V) showing numerous absorption lines that arises from matter being ejected by the supergiant primary. Multiple absorption features indicates that the wind material is not smoothly distributed but rather concentrated in discrete condensations. The column density and velocity structure of the absorption components is estimated using a nonlinear least-squares fit procedure.
Results. We have identified four distinct absorption systems with rest frame velocities of –0.5, –8.4, –14.4, and –19.9 km s^{-1}. An additional component is seen in Al III at 7.8 km s^{-1} probably constraining the position of the hot companion. With a spherical outflow geometry we would obtain a time average mass-loss rate due to episodic events up to $\dot{M} = 10^{-5}\ M_\odot\ \mathrm{yr}^{-1}$. The continuous background flow leads to a significant smaller mass-loss rate of $3 \times 10^{-7}\ M_\odot\ \mathrm{yr}^{-1}$.
Conclusions. There are two alternative explanations for the observed features: Either a moderate continuous mass flow is accompanied by episodic mass-loss events forming concentric shells; or the continuous outflow is disturbed by discrete clumps due to instabilities or unknown ejection processes. As a consequence former mass-loss determinations should be interpreted with care.

Key words. binaries: visual – circumstellar matter – stars: mass-loss – stars: late-type – stars: individual: α Scorpii

1. Introduction

In recent years our knowledge of winds and mass loss of late type giants and supergiants has grown rapidly, mainly due to extensive UV observations with *IUE* and *HST*. Despite considerable theoretical and observational work, the mechanisms governing the mass outflow from these stars are still not well elucidated. Several physical processes have been discussed in the literature: Alfvén waves, stochastic shocks, acoustic or magnetoacoustic waves, dust driving through radiation pressure, and pulsation (see e.g. Lafon & Berruyer 1991; Willson 2000). An important task of high resolution spectroscopy is to identify empirical constraints for the theoretical concepts and to determine accurate mass-loss rates for reliable evolution models.

Owing to the lack of theoretically supported models we feel compelled to introduce a simplified description of the outflow scenario. As a consequence the empirical measurements of mass loss rates and wind velocities for individual cool stars are still very uncertain. However, the presence of a hot binary companion in the wind of a red supergiant provides an exceptional opportunity to determine the properties of the circumstellar envelope with high precision. The secondary (generally a main sequence B star) serves as a convenient probe for the extended atmosphere of the evolved star. The binary technique, first applied to the visual system α Her by Deutsch (1956), has been extended to spectroscopic binaries. From the diagnostic point of view ultraviolet observations are particularly valuable, since the complex spectrum of the giant star is negligible below ∼3000 Å. In the UV the observed spectrum is purely that of the companion with superimposed circumstellar and interstellar lines. The reader can find more detailed information on the binary concept and related topics in numerous reviews (e.g. Reimers 1987, 1989; Baade 1990; Carpenter 1992; Ahmad 1993; Harper 1996; Baade 1998, Harper 2001).

The methodology of the binary technique has also been applied with advantage to the Antares system in the optical spectral region (e.g. Kudritzki & Reimers 1978) as well as in the UV (Hagen et al. 1987). However, several key problems have affected earlier mass-loss studies of α Sco:

- what is effectively measured is the density (at least column density) in some limited parts of the envelope. The determination of the mass-loss requires a theoretical or semi-empirical model of the envelope. Generally, the flow is assumed to be spherically symmetric and in a steady state;
- the ionization structure of the circumstellar envelope is very complex and affects the line formation significantly. The existence of an ionizing B star produces a more or less extended H II region. However, the ionization structure is primarily determined by the a priori unknown mass-loss rate and the continuum flux of the B star;

⋆ Based on observations made with the NASA/ESA *Hubble Space Telescope*, obtained at the Space Telescope Science Institute, which is operated by the AURA, Inc., under NASA contract NAS 5-26555; and on observations with the *International Ultraviolet Explorer*.

- the location of the secondary along the line of sight has a crucial influence on the mass-loss determination (van der Hucht et al. 1980). Unfortunately the geometry of the Antares system is poorly known;
- in the UV spectrum of α Sco a number of metal lines show P Cygni-type profiles. These lines are formed by scattering of B star photons in the circumstellar envelope of the primary (Hagen et al. 1987). The analysis requires the solution of a multidimensional radiation transfer problem. The task is quite similar to line formation calculations for ζ Aur type binaries (e.g. Baade et al. 1996);
- all ground state lines suffer from interstellar absorption. In some cases the the lines are Doppler shifted on the emission components of the P Cygni profiles (Hagen et al. 1987). Hence, the spectral analysis has to exclude these lines or to consider the interstellar contribution and the circumstellar line formation adequately;
- the interpretation of the line-broadening velocity as unresolved chaotic motions in the microturbulence sense is probably an oversimplification. Large-scale flow patterns of different amplitudes imply velocity correlations which cannot be treated as isotropic microturbulence;
- the B star itself may have a wind. Though there are no mass-loss signatures of α Sco B, a weak but fast wind could have dynamical effects on the circumstellar matter. Colliding stellar winds may cause a shock front in the vicinity of the B star. Other effects as orbital movement of the M star, gravitational forces of the secondary, and the ionization shock front at the H I-H II region interface will also interfere with the outflow symmetry. But all these effects are of minor importance for the mass-loss studies (Kudritzki & Reimers 1978).

In recent years infrared observations have provided further constraints on the mass-loss process in α Sco. Both one-dimensional scans at 11 μm wavelength in 1985 (Bloemhof & Danen 1995) and observations with a two-element interferometer at 11.15 μm during 1989/1990 (Danchi et al. 1994) have found that the inner $\sim 1''$ is devoid of dust. In contrast Marsh et al. (2001) reported that a substantial fraction of the dust is within a radial distance of $\sim 0\farcs5$ from the star. As an obvious conclusion there has been an ejection in the mean time. The observations show a ring structure as well as discrete clumps. Marsh et al. (2001) have interpreted these results as indicating the presence of two ejected shells of approximately 50 and 200 AU from the central star. The physical origin of these shells and clumps is yet unknown. There are several scenarios that could explain the observations. Pulsationally driven outflow models as well as instabilities or sporadic ejection processes in connection with large convective cells may be conceivable. Indeed, interferometric observations in the optical spectral range with the William Herschel Telescope show evidence for asymmetric structures on the stellar surface (Tuthill et al. 1997). These unresolved features, or hotspots, have timescales of 3 to 9 months consistent with a convective origin. These observations can also explain the irregular variability of Antares.

We have used the Goddard High-Resolution Spectrograph (*GHRS*) on the *Hubble Space Telescope* to study the structure of the outer envelope of α Sco. The high spectral resolution allows construction of a tentative model for the absorbing material. The goals of this study include the acquisition of information on the envelope structure, the wind kinematics, the binary geometry, and the gas depletion onto dust grains.

Table 1. Stellar parameters of α Sco.

Parameter	Value	Source
$R_{\rm M}$	22.2 mas	Bester et al. (1996)
	883 $R_\odot$	
$M_{\rm M}$	12.4 $M_\odot$	El Eid (1994)
$T_{\rm eff,M}$	3500 K	Bester et al. (1996)
$T_{\rm eff,B}$	18 500 K	Kudritzki & Reimers (1978)
Distance	185 pc	Perryman et al. (1997)
Separation	$2\farcs86$	McAlister et al. (1990)
	128.8 $R_{\rm M}$	
	529 AU	

2. Observations and stellar parameters

α Sco B was observed 1995 September 17 (GO program 5952) with the *GHRS* echelle gratings. Exposures were made for 30 wavelength settings, dictated by the position of $\sim$100 important wind and interstellar lines. The width of each region varies from $\sim$6 Å to $\sim$17 Å. The spectra have a resolution of approximately 3.5 km s^{-1} and a typical signal-to-noise ratio (S/N) of 30–40.

The observations are completed with SPYBAL exposures to improve the standard wavelength calibration. However, the accuracy of the wavelength scale depends on the magnitude of the relative thermal and magnetic drift and carousel positioning errors. Unfortunately the use of the Large Science Aperture (LSA) produces a nominal maximum error of 1.5 diodes which is equivalent to 4.5 km s^{-1} (Heap et al. 1995).

Table 1 lists the stellar parameters used in this study. Some fundamental aspects should be discussed in detail.

Kudritzki & Reimers (1978) and most of the following authors postulate a distance of 180 pc. This value is in good agreement with parallax in the Hipparcos Catalogue (Perryman et al. 1997) of 5.4 mas, i.e. 185 pc.

The most reliable angular diameter of the stellar disk of α Sco A has been determined at midinfrared wavelength (11 μm) using long-baseline interferometry (Bester et al. 1996). The value of 44.4 mas is slightly larger than measurements at visible wavelengths (e.g. Richichi & Lisi 1990), consistent with expected limb darkening effects in the visible region. The corresponding effective temperature is approximately 3500 K using the total luminosity of White (1980). With the Hipparcos distance of 185 pc the stellar radius becomes 883 $R_\odot$.

The projected angular separation of the two components changed between 1854 and 1989 from $3\farcs3$ (Hopmann 1958) to $2\farcs86$ (McAlister et al. 1990). The latter value corresponds to a projected linear separation of $p = 128.8\,R_{\rm M}$ or 529 AU (assuming a distance of 185 pc). The availability of very precise angle measurements of both the stellar radius and the separation facilitates the construction of a reliable geometric model. However, the time basis is not sufficient to establish a proper orbital solution.

Evolutionary models of α Sco A yield a mass of 12.4 $M_\odot$ and a surface gravity of $\log g = 0.1$ (El Eid 1994). Considering the mass loss Antares can be well described by a model of initially 15 $M_\odot$ evolved beyond core He-burning.

The true radial velocity of α Sco A cannot be determined exactly, since periodic and stochastic velocity variations are superposed on the stellar movement. For that reason the mean value of -3.4 km s^{-1} (Evans 1967) should be interpreted with care. Most authors prefer a value of -3 km s^{-1} which we also adopt for the present work. Smith et al. (1989) have found evidence of a period

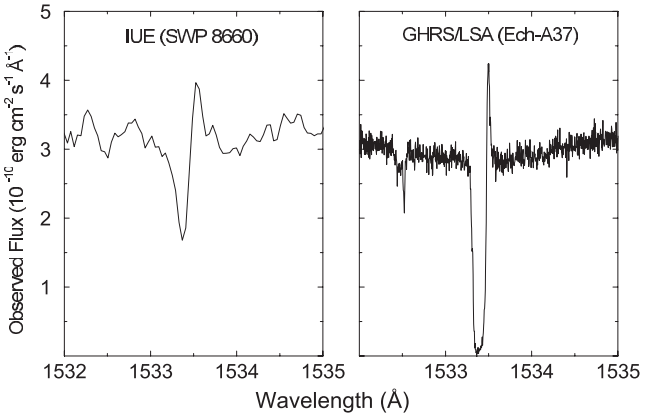

Fig. 1. Si II UV mult. 2 wind line observed with IUE (*left panel*) and *HST/GHRS* (*right panel*).

of 260 days and also a long-term signature of 7.35 yr. Like most M supergiants α Sco is an intrinsic variable with an amplitude of about $V = 0.9-1.8$ mag (van der Hucht et al. 1980). However, the published parameters of the variability differ considerably. Percy et al. (1996) report a period of 350 days and an additional time scale of several thousand days. It is controversial whether the radial-velocity periodicities coincide with the light curve variations.

3. Line profile analysis

The *HST* spectra of α Sco B (B2.5 V) show numerous lines of O I, Mg II, Al II, Al III, Si II, S II, Ti II, Cr II, Mn II, Fe II, Ni II, Cu II, and Zn II which can be interpreted as circumstellar absorption lines arising from matter being ejected by the supergiant primary α Sco A (M1.5 Iab). Nearly all spectral features clearly show multiple absorption components indicating that the wind material is not smoothly distributed but rather concentrated in discrete condensations. All circumstellar ground state lines suffer from interstellar absorption which cannot be seen separately. Additionally we can identify purely interstellar lines of C I and Mg I.

The strong emission features observed with *IUE* (Hagen et al. 1987) are weak or completely absent in the *HST* spectra. This behaviour is a consequence of different aperture sizes of the instruments (*IUE* large aperture: $10'' \times 20''$; *HST/GHRS* large science aperture [LSA]: $2'' \times 2''$). The volume of the emitting region is large compared to the scale of the orbit. Baade et al. (1996) have shown that very distant parts of the envelope can contribute to the line profile. The differential scattering effect becomes noticeable since the α Sco system is very extended (the binary separation is $\sim 2\farcs9$). In Fig. 1 we show a comparison of a typical wind line observed with both instruments. Even in strong lines the emission component is negligible or has only minor effects on the absoption line analysis.

3.1. Multi component fits

Our analysis was carried out using a multi component fit procedure to determine the parameters $v_{\rm comp}$ (radial velocity of the specific component), N (column density), and $v_{\rm b}$ (line broadening velocity) for each absorption dip. A continuous background absorption can be optionally added introducing the fit parameters $\dot{M}$ (mass-loss rate), $v_{\rm wind}$ (terminal wind velocity), and $v_{\rm b}$ (stochastic velocity or microturbulence). We have written a FORTRAN program based on the Levenberg-Marquardt algorithm to solve this nonlinear regression problem (see, e.g., Bevington & Robinson 2002). We have included additional parameters describing the local continuum curvature by a low order Legendre polynomial. A free floating continuum is a prerequisite for an adequate profile decomposition in the case of complex line ensembles.

For an adequate analysis it is also vital to correct for instrumental broadening during the fit procedure, i.e., each proposed fit has to be convolved with the instrumental profile of the Echelle spectrograph. The Echelle LSA line spread function is assumed to be well represented by a Gaussian of 4.4 pixels FWHM (Gilliland 1994). The convolution of the intrinsic spectrum and the instrumental spread function $P(\Delta\lambda)$ can be written:

$$F(\lambda) = P(\Delta\lambda) \otimes \left\{ F_{\rm c}(\lambda) \prod_i \exp[-\tau_i(\lambda, \lambda_0, N, v_{\rm b})] \right\}. \quad (1)$$

To improve the numerical efficiency of the nonlinear fit procedure we have to provide adequate initial parameters. In some cases good starting parameters are a precondition for the success of the fitting, since the algorithm tends to converge to the nearest, not necessarily global, minimum of the chi-square merit function. A first approximation can be found neglecting the *GHRS* instrumental profile and converting the flux profile into apparent optical depths using the relation

$$\tau_{\rm a}(v) = \ln[F_0(v)/F(v)], \quad (2)$$

where $F_0(v)$ and $F_{\rm obs}(v)$ are the background and the observed line flux at velocity v, respectively. If the instrumental resolution is high compared to the line width, $\tau_{\rm a}(v)$ will be a good representation of the true optical depth $\tau(v)$. However, an ill-defined continuum level or saturation effects may produce large uncertainties. The apparent optical depth can be fitted with a sum of Gaussians, each having a variable position, amplitude, and width.

If the program fails to converge on a reasonable model, the parameters can be adjusted by hand. In this way the fit can be modified to be acceptable by eye and then re-minimized. In some exceptional cases this procedure is the only chance to free a converged solution from a local chi-square minimum. The fit procedure for each absorption line is organized in four steps:

- transformation of the wavelength scale into a velocity scale relative to the M star;
- multi component Gaussian fit of the apparent optical depth of the absorption line $\tau_{\rm a}(v)$;
- multi component profile fit of the blurred Gaussian absorption line ensemble $\exp[-\tau(v)] \otimes P(v)$, where $P(v)$ denotes the instrumental profile;
- multi component fit of the Gaussian absorption line ensemble plus an underlying broad wind component and varying continuum.

Some theoretical profiles are shown superimposed on the observed spectra in Fig. 2. We apply a radial velocity of -3 km s^{-1} to transform the heliocentric velocity into the rest frame of the supergiant. However, the metallic velocity curve clearly shows a long-term variation, which hides the true radial velocity (Smith et al. 1989). This might be the main error of relating the absorption components to spatial positions. The rotational velocity of α Sco B is large, allowing circumstellar and stellar lines to be readily separated. In Tables 2 and 3 we summarize the results of the multi component fits. For the oscillator strengths we have used the new compilation of Morton (2003). The small velocity descrepancies between the components of different lines as

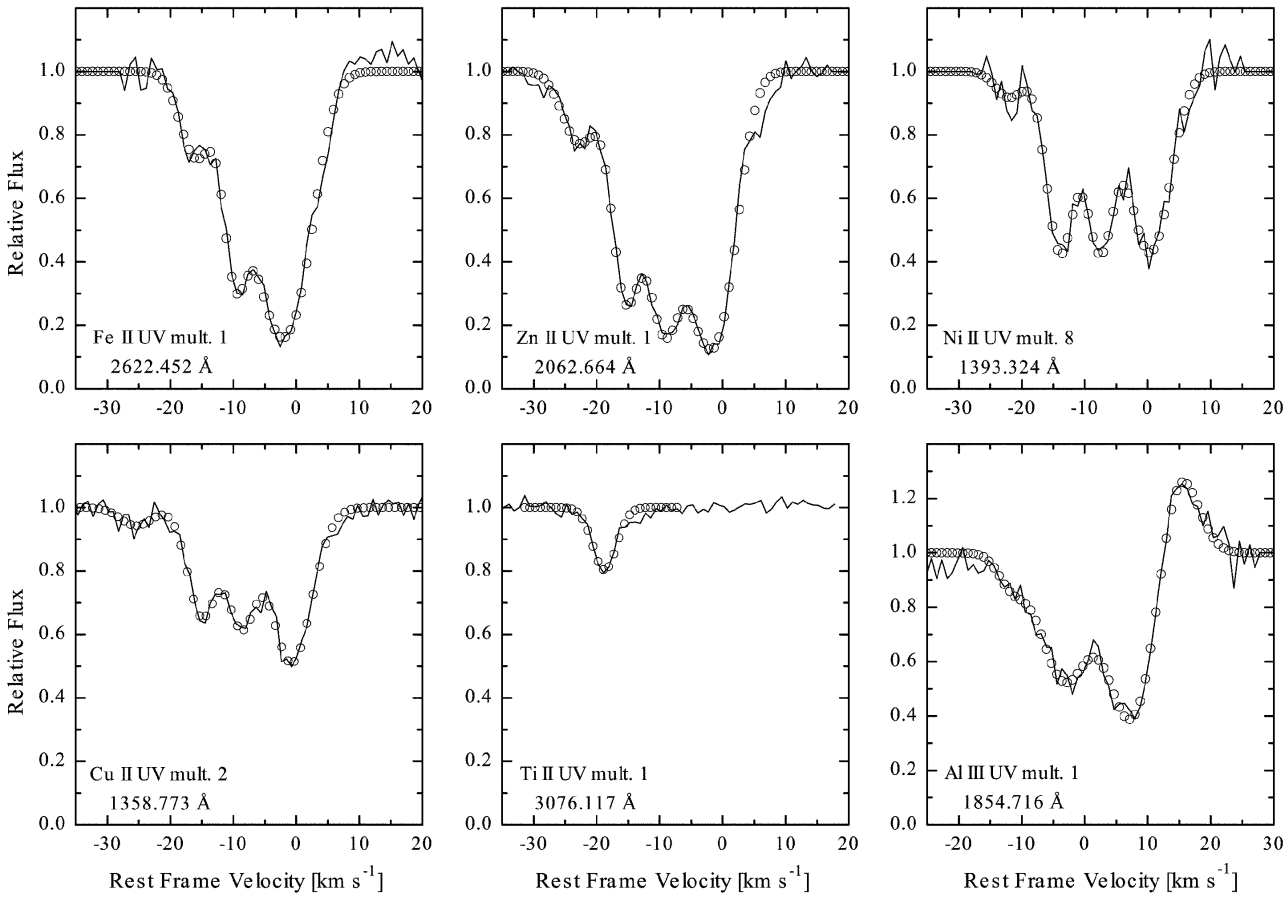

Fig. 2. Sample *HST* spectra of α Sco B with best fit multi-component models (open circles). The velocity scale applies to the rest frame of the supergiant.

seen in Fig. 2 are probably due to the use of the LSA. Averaging all observed lines the resulting velocity error could be reduced significantly. Nevertheless, the purely statistical errors given in Table 2 should be interpreted with care.

Our approach neglects reemission effects which cause P Cygni-type line profiles. Hagen et al. (1987) have shown that a pure absorption model may lead to erroneous mass loss rates using IUE spectra. Nevetheless this approximation seems to be justified in the case of *HST/GHRS* observations, since the LSA aperture is significantly smaller than the IUE aperture resulting in minor emission components. However, in some cases the remaining reemission features would cause erroneous column densities filling in the absorption troughs. With a correction procedure simulating the emission peaks by Gaussians this effect can be considered approximately, since the red wing of the emission line is clearly defined.

In cases where the absorption components are apparently unresolved and the line appears to be saturated, we perform simultaneous fits using different lines of the same species or we try to fit the profiles with fixed velocity parameters (i.e. the parameters $v_{\rm comp}$ and $v_{\rm b}$ are assumed to be known). The latter procedure guarantees convergence, but the resulting error bars are still very large. Another effect has to be considered for the ground state lines: the interstellar absorption may affect the column density determination of component 1. Observations of interstellar lines of neighbouring stars suggest that up to 30% of the equivalent width may be interstellar instead of circumstellar. As a consequence the column densities of component 1 has to be regarded as an upper limit.

Table 2. Kinematic structure.

Component	$v_{\rm comp}$ (km s^{-1})	$v_{\rm b}$ (km s^{-1})
0	7.8 ± 0.2	2.0 ± 0.2
1	-0.5 ± 0.2	4.3 ± 0.2
2	-8.4 ± 0.2	2.2 ± 0.2
3	-14.4 ± 0.2	2.0 ± 0.1
4	-19.9 ± 0.3	2.0 ± 0.2

There is also evidence of a continuous outflow signature. In order to model this smooth wind component we have to integrate the optical depth along the ray to the observer explicitely:

$$\tau(\lambda) = \int_{z_{\rm min}}^{z_{\rm max}} \kappa(z)\phi(z,\lambda){\rm d}z, \tag{3}$$

where z denotes the distance along the line of sight measured from the plane defined by the M star, $\kappa(z)$ is the opacity, and $\phi(z,\lambda)$ the Gaussian profile function. The integration limit $z_{\rm min}$ is defined by the position of the B star or, physically more realistic, the boundary of the H II region in direction to the observer. The other limit $z_{\rm max}$ is chosen so large that the calculated lines do not vary any longer. The profile function contains the velocity gradient and can be written as

$$\phi(z,\lambda) = \frac{1}{\sqrt{\pi}} \exp\left[-\left(\lambda + \frac{\lambda_0 v_{\rm wind}}{c}\frac{z}{r} - \lambda_0\right)^2 / \Delta\lambda_{\rm D}^2\right], \tag{4}$$

Table 3. Column densities with fitting errors (the components marked with IS suffer from interstellar absorption and provide only upper limits).

Ion	Level	Comp.	log *N*	
O I	158 cm^{-1}	1	14.77 (+0.10, −0.13)	
		2	13.92 (+0.12, −0.17)	
		3	14.24 (+0.07, −0.09)	
		4	12.79 (+0.06, −0.06)	
	227 cm^{-1}	1	14.49 (+0.13, −0.19)	
		2	14.19 (+0.24, −0.57)	
		3	14.15 (+0.06, −0.07)	
		4	12.52 (+0.11, −0.15)	
Mg II	0 cm^{-1}	1	15.83 (+0.03, −0.04)	IS
		2	15.71 (+0.08, −0.10)	
		3	15.62 (+0.03, −0.03)	
		4	14.86 (+0.06, −0.07)	
Al II	0 cm^{-1}	1	14.65	IS
		2	13.74	
		3	14.35	
		4	14.14	
Al III	0 cm^{-1}	0	12.54 (+0.28, −0.97)	
		1	12.32 (+0.02, −0.02)	
		2	11.48 (+0.09, −0.12)	
Si II	0 cm^{-1}	1	15.18 (+0.02, −0.02)	IS
		2	15.28 (+0.07, −0.09)	
		3	14.93 (+0.04, −0.05)	
		4	14.57 (+0.02, −0.02)	
	287 cm^{-1}	1	14.45 (+0.31, −1.60)	
		2	13.61 (+0.10, −0.13)	
		3	13.24 (+0.16, −0.26)	
		4	12.42 (+0.22, −0.49)	
S II	0 cm^{-1}	1	15.32 (+0.06, −0.07)	
		2	15.21 (+0.12, −0.17)	
		3	14.88 (+0.07, −0.08)	
		4	14.68 (+0.04, −0.05)	
Ti II	0 cm^{-1}	3	11.50 (+0.06, −0.07)	
		4	12.05 (+0.04, −0.04)	
	94 cm^{-1}	4	12.05 (+0.02, −0.02)	
	226 cm^{-1}	3	11.47 (+0.05, −0.06)	
		4	11.91 (+0.03, −0.04)	
Cr II	0 cm^{-1}	1	13.92 (+0.02, −0.02)	IS
		2	13.96 (+0.07, −0.09)	
		3	13.77 (+0.04, −0.05)	
		4	12.98 (+0.02, −0.02)	
Mn II	0 cm^{-1}	1	13.26 (+0.07, −0.09)	IS
		2	13.38 (+0.08, −0.10)	
		3	13.17 (+0.11, −0.15)	
		4	12.52 (+0.03, −0.03)	

Table 3. continued.

Ion	Level	Comp.	log *N*	
Fe II	0 cm^{-1}	1	14.40 (+0.12, −0.16)	IS
		2	14.57 (+0.37, −0.49)	
		3	13.60 (+0.19, −0.34)	
		4	13.70 (+0.18, −0.30)	
	385 cm^{-1}	1	14.48 (+0.01, −0.01)	
		2	14.13 (+0.07, −0.08)	
		3	13.56 (+0.06, −0.07)	
		4	11.93 (+0.08, −0.09)	
	668 cm^{-1}	1	14.23 (+0.02, −0.02)	
		2	13.60 (+0.06, −0.07)	
		3	13.16 (+0.03, −0.03)	
		4	13.33 (+0.08, −0.10)	
	863 cm^{-1}	1	14.13 (+0.02, −0.02)	
		2	13.44 (+0.03, −0.04)	
		3	12.83 (+0.04, −0.04)	
	977 cm^{-1}	1	13.61 (+0.01, −0.01)	
		2	13.19 (+0.11, −0.14)	
		3	12.69 (+0.04, −0.04)	
	1873 cm^{-1}	1	14.36 (+0.04, −0.04)	
		2	13.66 (+0.05, −0.05)	
		3	13.39 (+0.03, −0.03)	
		4	12.21 (+0.14, −0.21)	
	2430 cm^{-1}	1	13.63 (+0.02, −0.02)	
		2	12.67 (+0.04, −0.05)	
		3	12.03 (+0.09, −0.12)	
	2838 cm^{-1}	1	13.44 (+0.05, −0.06)	
		2	12.37 (+0.08, −0.10)	
		3	12.27 (+0.10, −0.14)	
	3117 cm^{-1}	1	13.11 (+0.08, −0.10)	
Ni II	0 cm^{-1}	1	14.30 (+0.02, −0.02)	IS
		2	14.21 (+0.04, −0.04)	
		3	14.18 (+0.03, −0.04)	
		4	13.27 (+0.01, −0.02)	
Cu II	0 cm^{-1}	1	12.72 (+0.02, −0.02)	IS
		2	12.43 (+0.04, −0.04)	
		3	12.40 (+0.04, −0.04)	
		4	11.60 (+0.09, −0.12)	
Zn II	0 cm^{-1}	1	13.07 (+0.03, −0.03)	IS
		2	12.79 (+0.13, −0.19)	
		3	12.74 (+0.04, −0.04)	
		4	11.94 (+0.06, −0.07)	

where $\Delta\lambda_D$ denotes the Doppler width and v_{wind} the expansion velocity. It can be assumed that the wind has reached its final speed along the whole line of sight. The true radial distance from the supergiant is $r = \sqrt{p^2 + z^2}$. Following the stationary equation of mass conservation the density variation is given by

$$n_H(r) = \frac{\dot{M}}{4\pi r^2 \mu_H m_H v_{wind}}, \quad (5)$$

where μ_H represents the mean atomic weight per hydrogen nucleus. In this work we take $\mu_H = 1.4$.

The consideration of an underlying wind component can explain some minor features in the line profiles. In Fig. 3 we compare a four-component model with a three-componet approach plus underlying wind profile. To demonstrate the difference in the quality we introduce a goodness-of-fit parameter (e.g. Press et al. 1992)

$$q = Q\left(\frac{\nu}{2}, \frac{\chi^2}{2}\right), \quad (6)$$

where Q represents the incomplete gamma function and ν is the number of degrees of freedom. The value of q should not be overinterpreted, but if it is larger than 0.1 then the fit model is believable and a larger goodness-of-fit parameter points out a more reliable solution. The existence of a continuous outflow component is also supported by the occurrence of a pronounced emission profile (Hagen et al. 1987). The wind features are visible in several lines and yield an estimate of the continuous mass-loss rate (see Sect. 3.2).

It should be pointed out that some profiles have a strange appearance. The Al III line arises in a region near the B star and is seen in the components 1 and 2. An additional absorption component is observed at 7.8 km s^{-1} which we label with 0. Ti II is only visible in component 4 and with a very weak signature in component 3. The weakness or lack of the Ti lines is probably

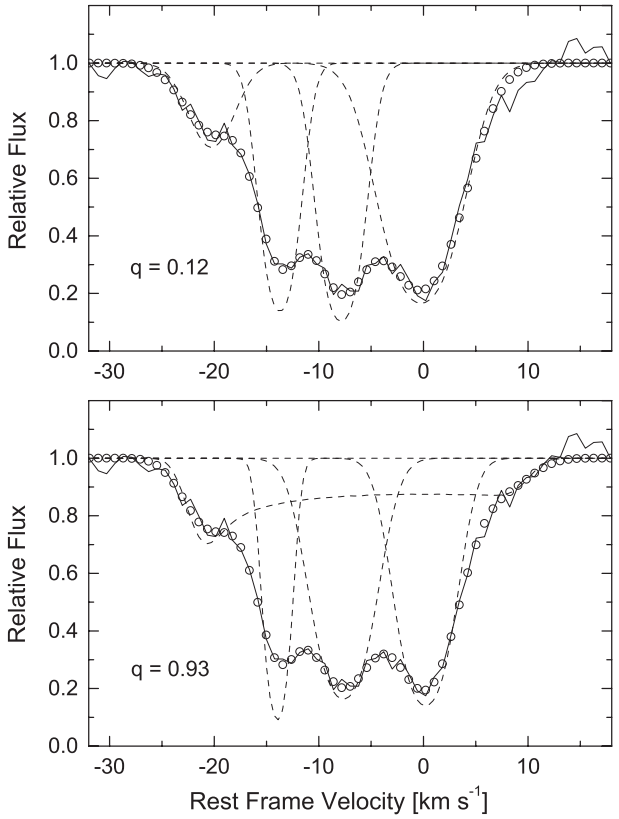

Fig. 3. Mg II UV mult. 1 wind line. *The upper panel* shows a four component fit (solid line: observation, open circles: model). *The lower panel* depicts a three-component fit with wind model ($\dot{M} = 2.6 \times 10^{-7}\ M_\odot\,\mathrm{yr}^{-1}$). The quantity q is the goodness-of-fit parameter (see text).

due to dust depletion. All other ions show a four-component structure partly obscured by saturation effects in the strong lines. Recent observations of the stronger Ti II lines in the optical UV using *UVES* at the *VLT* confirm this finding for Ti II (Reimers et al., in preparation).

3.2. Column densities, mass outflow, and velocity distribution

The population of the ground state levels are controlled by three processes: particle collisions, direct excitation via infrared photons, and indirect excitation due to ultraviolet pumping (e.g. Bahcall & Wolf 1968). Since the physical conditions vary considerably in the envelope, we expect a systematic change of the fine-structure population. Large electron densities as well as strong UV fluxes near the B star will cause a Boltzmann distribution, i.e., the ground state levels are populated according to the statistical weights. However, in the outer envelope these excitation mechanisms become more and more ineffective and only the lowest fine-structure component is occupied. These physical effects are clearly reflected by our data (see Table 3).

To interpret the line-of-sight column densities we need accurate information on the location of α Sco B relative to the primary. Kudritzki & Reimers (1978) place the B star 235 $R_{\rm sg}$ or 625 AU closer than the M star. This corresponds to a position angle (the angle between the plane of the sky and the line joining the stars) of 50° toward the sun. Using spectroscopic arguments van der Hucht et al. (1980) suggest a position of the B star of 782 AU or 56° in front of the plane of α Sco A. As a best fit to the radio data, Hjellming & Newell (1983) find a position angle of 24° and noticed an inconsistency with the former results. Radio continuum observations, however, do not contain velocity information and cannot distinguish between a location in front or behind the plane of the sky.

This discrepancy also appears considering the sequence of absorption components observed with *HST*. The spectral features suggest a position of the B star at or more likely beyond the distance of α Sco A. In the M star's rest frame the first absorption dip of singly ionized metals occurs at approximately $-0.5\,\mathrm{km\,s^{-1}}$. Assuming an outflow velocity of $20\,\mathrm{km\,s^{-1}}$ the nearest position is 3.3 supergiant radii or 13 AU in front of the plane. However, near the B star we expect significant ionization effects, i.e., an H II region is formed and some metals may be doubly ionized. Indeed, Al III is observed with an absorption component at $7.8\,\mathrm{km\,s^{-1}}$ implying a position of $56\,R_{\rm sg}$ or 224 AU behind the M star equivalent to a position angle of 23°.

Using this binary configuration and a radial outflow scenario we are able to establish a geometrical model of the circumstellar absorbers. We use the following notation: r denotes the radial distance of a specific absorber, p is the projected separation of the two stars (also called impact parameter), and z the distance along the line of sight measured from the plane defined by the M star. If we assume a uniform outflow speed identifying the absorber velocity with the ejection velocity $v_{\rm e}$ the projected velocity of each absorber can be written $v_{\rm comp} = v_{\rm e}\,z/r$. In this way the true distance from the M star can be estimated considering the velocity of each absorption component:

$$r = \frac{v_{\rm e}\,p}{\sqrt{v_{\rm e}^2 - v_{\rm comp}^2}}. \tag{7}$$

In the case of clumps of unknown size it is impossible to transform the column densities into volume densities or masses. To estimate the mass of the absorbing material we use a simple shell model giving an upper limit of the ejected material. Indeed the observed infrared features suggest a concentric shell structure. If we assume thin shells we can correct the measured column density for its radial values: $N_{\rm radial} = N_{\rm obs}\,z/r$. The total number of atoms of an observed species is given by $N_{\rm tot} = 4\pi r z N_{\rm obs}$. Finally we can estimate the total mass in the gas phase contained in the shell:

$$\begin{aligned} M_{\rm shell} &= \frac{N_{\rm tot,X}}{({\rm X/H})_{\rm g}}\mu_{\rm H}\,m_{\rm H} \\ &= 4\pi r z \frac{N_{\rm obs,X}}{({\rm X/H})_{\rm g}}\mu_{\rm H}\,m_{\rm H}, \end{aligned} \tag{8}$$

where $({\rm X/H})_{\rm g}$ is the gas phase abundance of element X relative to hydrogen. The total mass of a shell can only be estimated for the second and third absorption zone. For the other components the approximation would be inadequate. Including the depletion correction (see Sect. 3.3) the shell model leads to $6.4 \times 10^{-5}\,M_\odot$ for the second shell and $1.7 \times 10^{-4}\,M_\odot$ for the third absorber. Only these shells can be used to quantify the episodic mass loss. The ejection history prior to component 1 is unknown and the component 4 has probably to be identified with the steady mass-loss process.

To estimate the time scale of the mass outflow we have calculated the wind travel time between successive absorbers:

$$\begin{aligned} T_{i,i+1} &= \frac{r_{i+1} - r_i}{v_{\rm e}} \\ &= p\left[\left(v_{\rm e}^2 - v_{i+1}^2\right)^{-1/2} - \left(v_{\rm e}^2 - v_i^2\right)^{-1/2}\right]. \end{aligned} \tag{9}$$

Table 4. Travel time between successive shells assuming different ejection velocities.

v_e	20	25	30	50	km s^{-1}
$T_{\star 1}$	122	98	81	49	yrs
T_{12}	12.4	6.0	3.4	0.70	yrs
T_{23}	41.4	15.8	8.0	1.5	yrs
T_{34}	1046	41.9	16.0	2.2	yrs

The result depends strongly on the ejection velocity of the absorbing material. In Table 4 we present the travel time for different velocities. The time scale is relatively short and should be compared to radial-velocity periodicities and brightness variations. In the literature one can find light and radial-velocity periods (e.g. Smith et al. 1989; Percy et al. 1996) that have the same order of magnitude as the travel time. It is, however, difficult to see whether pulsations or stochastic velocity fluctuations are responsible.

A significant continuous mass outflow is a main feature of stars above the Linsky-Haisch dividing line in the HRD. Indeed, the wind of Antares has been studied over decades assuming a smooth expansion in spherical symmetry with respect to the M supergiant. There is direct evidence for the continuous outflow scenario. Hagen et al. (1987) have modeled P-Cygni type line profiles with a spherically symmetric wind considering the re-emission effects adequately. Indeed, these lines can only be explained by the existence of an extended scattering region. The embedded hot B star companion causes an H II region that can be regarded as subregion of the wind. The ionized cavity produces radio emission which has been observed with the VLA (Hjellming & Newell 1983). Both the radio maps and the brightness temperature are consistent with a wind model. The mass-loss rate of the different studies varies between 1×10^{-7} and $6 \times 10^{-6}\ M_\odot\ \mathrm{yr}^{-1}$. However, a direct comparison is not possible, since the methodical approaches as well as stellar data, oscillator strengths, abundances, etc. are inconsistent. Furthermore it is possible that transient absorption features have affected the respective analyses.

In our observations from 1995 the multicomponent character is very pronounced. As we have described in Sect. 3.1 the continuous mass outflow may be visible in some minor features. Only few lines are really appropriate to measure this continuous fraction. Assuming solar abundance the correspondent fits yield mass-loss rates of $2.6 \times 10^{-7}\ M_\odot\ \mathrm{yr}^{-1}$ (Mg II), $1.9 \times 10^{-7}\ M_\odot\ \mathrm{yr}^{-1}$ (Mn II), $2.2 \times 10^{-7}\ M_\odot\ \mathrm{yr}^{-1}$ (Ni II), and $5.5 \times 10^{-7}\ M_\odot\ \mathrm{yr}^{-1}$ (Zn II) with a mean value of $3 \times 10^{-7}\ M_\odot\ \mathrm{yr}^{-1}$ in apparently good agreement with former wind studies. Possibly the lower rates of Mg, Mn, and Ni are due to dust depletion (see next section). As a by-product of the fit procedure we obtain a terminal wind velocity of 23.3 km s^{-1}. Additionally the inner boundary of the line of sight defines the closest possible position of the B star companion. A simultaneous fit yields 240 ± 20 AU which agrees with the position of the Al III absorption.

It is difficult to specify the episodic mass-loss rate reliably. Following the shell scenario of the intermittent ejection processes the resulting mass loss will exceed the continuous outflow portion considerably. Combining Eqs. (8) and (9) the effective mass-loss rate can be defined as $\dot{M}_{\mathrm{eff},i} = M_{\mathrm{shell},i}/T_{i-1,i}$. As mentioned above only the absorption zones 2 and 3 provide information to quantify effective mass-loss rates. Under the assumption that the ejection velocity is similar to the continuous wind velocity between 20 and 25 km s^{-1} we obtain $\dot{M}_2 = (5.2 \times 10^{-6}\text{–}1.1 \times 10^{-5})\ M_\odot\ \mathrm{yr}^{-1}$ and $\dot{M}_3 = (4.1 \times 10^{-6}\text{–}1.1 \times 10^{-5})\ M_\odot\ \mathrm{yr}^{-1}$. Though we should not over-interpret the result a value up to $1 \times 10^{-5}\ M_\odot\ \mathrm{yr}^{-1}$ may be reached strongly dependent on the true ejection velocity. A lower limit of $5 \times 10^{-6}\ M_\odot\ \mathrm{yr}^{-1}$ may be specified though it cannot be ruled out that the ejection velocity is lower than the maximum observed speed. In this case Eqs. (7) to (9) break down and no reliable estimate is possible.

Unfortunately the mass-loss process cannot be resolved, i.e., the spectra do not allow to estimate the instantaneous mass-loss rate during the ejection episodes. Both the typical duration of an enhanced mass-loss event and the density distribution of the expanding shells elude the observation. Without having a reliable ejection model it is impossible to translate the derived column densities into true volume densities. As a consequence there is no information about the density contrast between the continuous wind and the condensed shells.

All former studies were based on spectra which did not resolve the profile structure adequately. Therefore these wind analyses have provided artificial mass-loss rates based on erroneous model assumptions. The first quantitative study by Kudritzki & Reimers (1978), in particular, was based on the Ti II lines which, as we have learned from the *HST* spectra, are seen only in the usually weak component 4.

3.3. Circumstellar depletion and interstellar lines

Having derived the column densities we are able to estimate the abundances and the depletion in the circumstellar material producing the discrete absorption lines. Owing to the lack of precise knowledge of the hydrogen column density we introduce the differential depletion

$$\left[\frac{\mathrm{X}}{\mathrm{Zn}}\right] = \lg\left(\frac{N_{\mathrm{X}}}{N_{\mathrm{Zn}}}\right) - \lg\left(\frac{N_{\mathrm{X}}}{N_{\mathrm{Zn}}}\right)_\odot . \quad (10)$$

We use zinc as reference element, since Zn seems to be very little depleted or even undepleted in both the circumstellar and diffuse cloud environment (Cardelli 1984; Snow et al. 1987). Our results for α Sco are shown in Fig. 4. For the solar abundances we use the compilation of Palme & Jones (2003).

The depletion pattern is a complex interplay between element depletion by grain condensation and radiation effects. Indeed, the presence of the B star in the α Sco system might inhibit the formation of grains in large parts of the envelope. In addition the strong ultraviolet flux forms an H II region and can even produce doubly ionized metals (Hagen et al. 1987). Figure 4 demonstrates that the depletion pattern only roughly follows the interstellar depletion pattern. Generally the circumstellar depletions are significantly less than the galactic diffuse depletions. We have omitted the first component, since it is contaminated by interstellar absorption.

In the available *GHRS* observation which merely covers a small part of the UV spectrum we can only identify interstellar lines of C I with $\log N = 13.9$ and Mg I with $\log N = 13.7$ with a mean position of -2.1 km s^{-1} . The interstellar components of the ground state lines of singly ionized species cannot be resolved, so that component 1 is significantly contaminated. This effect has to be regarded as a disturbing factor in the analysis, since an ad hoc correction of the column densities would be error-prone.

4. Results and conclusions

This work is based on *HST/GHRS* observations of α Sco B observed 1995 September 17 (GO program 5952). The spectra

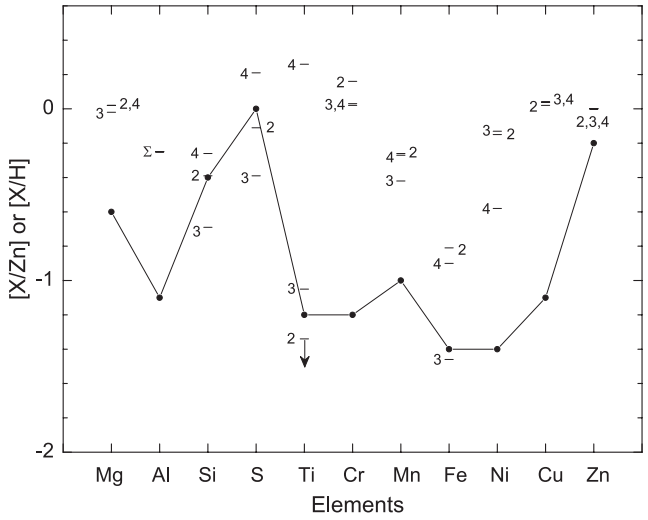

Fig. 4. Circumstellar depletion of absorption components 2–4. The depletion is given in its differential form (see Eq. (10)). The three absorption components are depicted separately and labelled according to the definition in Table 3. For Al, Si, S, and Fe the derived column densities (and hence the depletion) are uncertain, since the ground state lines are mainly saturated. Additionally the first component is filled in with re-emission. For aluminium we can merely specify the mean depletion. The weak inner components of Ti II define an upper limit of the depletion. For comparison we present the galactic "warm cloud" depletion pattern (Welty et al. 1999).

show numerous lines which can be interpreted as circumstellar absorption lines arising from matter being ejected by the supergiant primary α Sco A. Below we summarize the main results of our analysis.

- The spectra show four distinct absorption components (plus one component only seen in Al III) indicating an episodic character of the supergiant's mass loss. Unknown ejection processes may form discrete clumps or shells which can be directly observed in mid-infrared observations of the circumstellar dust around α Sco (Marsh et al. 2001).
- There is also evidence of a moderate continuous outflow with a mass-loss rate of $3\times10^{-7}\,M_\odot\,\mathrm{yr}^{-1}$ as typical for stars of this spectral type. Observations of the re-emission components of scattering lines (Hagen et al. 1987) as well as radio observations of the H II region produced by the B star companion (Hjellming & Newell 1983) may serve as direct proofs.
- Without additional information about the responsible processes it is difficult to evaluate reliable rates for the episodic mass-loss component. Assuming concentric shells and ejection velocities between 20 and 25 km s^{-1} we can estimate effective mass-loss rates of $(5\times10^{-6}–1\times10^{-5})\,M_\odot\,\mathrm{yr}^{-1}$. These values should be only interpreted as an order-of-magnitude estimate. Apparently the continuous component plays a secondary role with an outflow rate of only $3\times10^{-7}\,M_\odot\,\mathrm{yr}^{-1}$. This is a mean value with a scatter of roughly a factor of two.
- The detectable absorption systems have rest frame velocities of –0.5, –8.4, –14.4, and –19.9 km s^{-1}. An additional component is seen in Al III at 7.8 km s^{-1} probably defining the position of the hot companion or the border of the H II region. However, the absolute velocities should be regarded with care, since there are significant differences for several wavelength settings due to the use of the LSA. The line broadening velocity lies between 2 and 4 km s^{-1}. It is yet unknown whether it reflects isotropic microturbulent motions or large-scale flow patterns implying velocity correlations.
- The time scale of the shell propagation is relatively short. It should be possile to observe significant changes of the absorption structure within few years. Indeed, infrared observations have supplied direct evidence that there are ejections within a period of one decade (Marsh et al. 2001). In the literature one can find light and radial-velocity periods (e.g. Smith et al. 1989; Percy et al. 1996) that have the same order of magnitude. However, it is not clear whether pulsations are essentially responsible for the mass ejection. It is also possible that the ejected material has its seeds in transient, large convective cells (e.g. Schwarzschild 1975). The latter scenario gets impetus from the detection of hotspots on late-type supergiants including α Sco (Tuthill et al. 1997).
- The geometry of the α Sco system has to be modified to be consistent with the observed features. The most probable configuration favors a B star position of more than 220 AU behind the M star in contrast to prior studies.
- The elements in the circumstellar material are depleted with respect to solar values. These depletions are most likely attributed to the formation of dust in the observed clumps or shells. However, the existence of strong UV radiation from the B star companion causes lower depletions than the average galactic diffuse values. The interplay between the formation of molecules or dust grains and the competing process of photo dissociation cannot be understood without a reliable model of the mass-loss scenario.

Our analysis has shown that the mass-loss process in α Sco is much more complex than previously thought. On basis of existing observations it is impossible to establish a reliable outflow scenario. As a consequence the mass-loss rate can only be quantified with a high degree of uncertainty. All previous mass-loss determinations should be considered with care, since it can be easily shown that a single-component analysis of unresolved absorption line ensembles leads to erroneous parameters.

The next step to unravel the mass-loss phenomenon of the M supergiant would be the compilation of new observations of the emission nebula in different spectral regions. High resolution long-slit exposures in the optical would create a 2D map of the envelope primarily observable in [Fe II] lines. These observation would allow to construct a reliable model of the wind and the embedded H II region. Indeed, the Antares nebula is the only known case where the wind of a red supergiant can be spatially resolved with high spectral resolution. Extending the method of Hjellming & Newell (1983) better multifrequency radio continuum observations may also help to measure the H II region as part of the supergiant's wind. Direct infrared observations could trace the evolution of the ejection processes and the formation of molecules and dust.

Acknowledgements. This work was supported in parts by the Verbundforschung of the Bundesministerium für Bildung, Wissenschaft, Forschung und Technologie under Grant No. 50 OR 96016. We made use of the ViziR search engine, a joint effort of CDS (Strasbourg, France) and ESA-ESRIN.

References

Ahmad, I. A. 1993, in The Realm of Interacting Binary Stars, ed. Sahade et al. (Dordrecht: Kluwer), 305
Baade, R. 1990, Winds in cool stars, in Evolution in Astrophysics, ed. E. J. Rolfe, ESA SP-310, 65
Baade, R. 1998, The outer structure of ζ Aur stars, in Ultraviolet Astrophysics, Beyond the IUE Final Archive, ed. B. Harris, ESA SP-413, 325
Baade, R., Kirsch, T., Reimers, D., et al. 1996, ApJ, 466, 979
Bester, M., Danchi, W. C., Hale, D., et al. 1996, ApJ, 463, 336

Bevington, P. R., & Robinson, D. K. 2002, Data Reduction and Error Analysis for the Physical Sciences (New York: McGraw-Hill)
Bloemhof, E. E., & Dannen, R. M. 1995, ApJ, 440, L93
Cardelli, J. A. 1984, AJ, 89, 1825
Carpenter, K. G. 1992, in Evolutionary Processes in Interacting Binary Stars, ed. Kondo et al. (Dordrecht: Kluwer), 51
Danchi, W. C., Bester, M., Degiacomi, C. G., Greenhill, L. J., & Townes, C. H. 1994, AJ, 107, 1469
Deutsch, A. J. 1956, ApJ, 123, 210
El Eid, M. F. 1994, A&A, 285, 915
Evans, D. S. 1967, IAUS, 30, 57
Gilliland, R. L. 1994, GHRS Instrument Science Report 063, Space Telescope Science Institute, Baltimore
Hagen, H.-J., Hempe, K., & Reimers, D. 1987, A&A, 184, 256
Harper, G. 1996, Mass-loss and Winds from Cool Giants, in 9th Cambridge Workshop on Cool Stars, Stellar Systems and the Sun, ASP Conf. Ser., 109, 481
Harper, G. 2001, Winds of Evolved Late-type Stars studied with the HST, in 11th Cambridge Workshop on Cool Stars, Stellar Systems and the Sun, ASP Conf. Ser., 223, 368
Heap, S. R., Brandt, J. C., Randall, C. E., et al. 1995, PASP, 107, 871
Hjellming, R. M., & Newell, R. T. 1983, ApJ, 275, 704
Hopmann, J. 1958, Mitt. Univ.-Sternw. Wien 9, 135
Kudritzki, R. P., & Reimers, D. 1978, A&A, 70, 227
Lafon, J.-P. J., & Berruyer, N. 1991, A&ARv, 2, 249
Marsh, K. A., Bloemhof, E. E., Koerner, D. W., & Ressler, M. E. 2001, ApJ, 548, 861
McAlister, H. A., Hartkopf, W. I., & Franz, O. G. 1990, AJ, 99, 965
Morton, D. C. 2003, ApJS, 149, 205
Palme, H., & Jones, A. 2003, Solar System Abundances of the Elements, in Treatise on Geochemistry, ed. A. M. Davis (Elsevier Pergamon), 1, 41
Percy, J. R., Desjardins, A., Yu, L., & Landis, H. J. 1996, PASP, 108, 139
Perryman, M. A. C., Lindegren, L., Kovalevsky, J., et al. 1997, A&A, 323, L49
Press, W. H., Teukolsky, S. A., Vetterling, W. T., & Flannery, B. P. 1992, Numerical recipes in FORTRAN, 2nd edn. (Cambridge University Press)
Reimers, D. 1987, What do binaries teach us about mass-loss from late-type stars? in Circumstellar Matter, ed. I. Appenzeller, & C. Jordan (Dordrecht: Reidel), IAU Symp., 122, 307
Reimers, D. 1989, Observations of the chromospheres, coronae, and winds of F, G, and K stars, in FGK stars and T Tauri stars, ed. L. E. Cram, & L. V. Kuhi, NASA SP-502, 53
Richichi, A., & Lisi, F. 1990, A&A 230, 355
Smith, M. A., Patten, B. M., & Goldberg, L. 1989, AJ 98, 2233
Snow, T. P., Buss, R. H., Gilra, D. P., & Swings, J. P. 1987, ApJ, 321, 921
Tuthill, P. G., Haniff, C. A., & Baldwin, J. E. 1997, MNRAS, 285, 529
van der Hucht, K. A., Bernat, A. P., & Kondo, Y. 1980, A&A, 82, 14
Welty, D. E., Hobbs, L. M., Lauroesch, J. T., et al. 1999, ApJS, 124, 465
Willson, L. A. 2000, ARA&A, 38, 573